Towards Field Driven Design of Cellular Materials for Energy Absorption: Modeling and Simulation of Variable-thickness Schwarz-P TPMS Structures

Mandar Shinde, Irving E. Ramirez-Chavez, Dhruv Bhate

3DX Research Group, Arizona State University, Mesa, AZ 85212

Abstract

The design, modeling and optimization of cellular materials for energy absorption remains one of the more challenging sub-domains within architected cellular and meta-materials for mechanical behavior. The work in this field is primarily of an empirical and experimental nature, with little use of modeling and simulation to drive design. Further, most of the work involves constant thickness cellular structures when there is ample evidence in nature and engineered foams that there are advantages to heterogeneity in thickness of the walls and struts that make up cellular structures. This gap can be attributed to the modeling challenges associated with accurately representing the large deformations and contact seen in cellular materials subjected to very large compressive strains. This in turn makes it difficult to implement non-empirical design, such as design emerging from a physics-based simulation. This work addresses this gap by proposing, developing, implementing and validating a continuum shell based finite element model that enables the simulation of the behavior of variable thickness Schwarz-P TPMS cellular structures. Four different fields: two rational (linear gradient and failure band) and two stochastic, are implemented and studied, with all showing improvements over the uniform thickness baseline. In so doing, the modeling approach for field driven design of variable thickness TPMS structures for energy absorption is demonstrated and validated for the first time.

Introduction

Outside of honeycomb panels used in a wide range of structures to leverage their high stiffness to weight ratios, cellular materials are most often used for energy absorption, ranging from crash structures in transportation to packaging materials. One of the challenges with studying energy absorption, which extends to the ability to design them, is that there is no single, easily measurable metric that allows one to determine what a good energy absorber constitutes [1]. The compression response of a cellular material typically takes the form of the stress-strain plot shown in Figure 1a. While energy absorption (per unit volume of the structure of interest) is nominally the area under the stress-strain curve, a practical energy absorber is seeking to absorb this energy while also staying below an acceptable stress level. The way to maximize energy absorption is to have a flat plateau and a late onset strain of densification, which itself is determined based on the peak efficiency achieved during compression, as shown in Figure 1b [2]. All of this must be achieved while keeping the maximum transmitted stress (MTS) below the acceptable stress threshold [3].

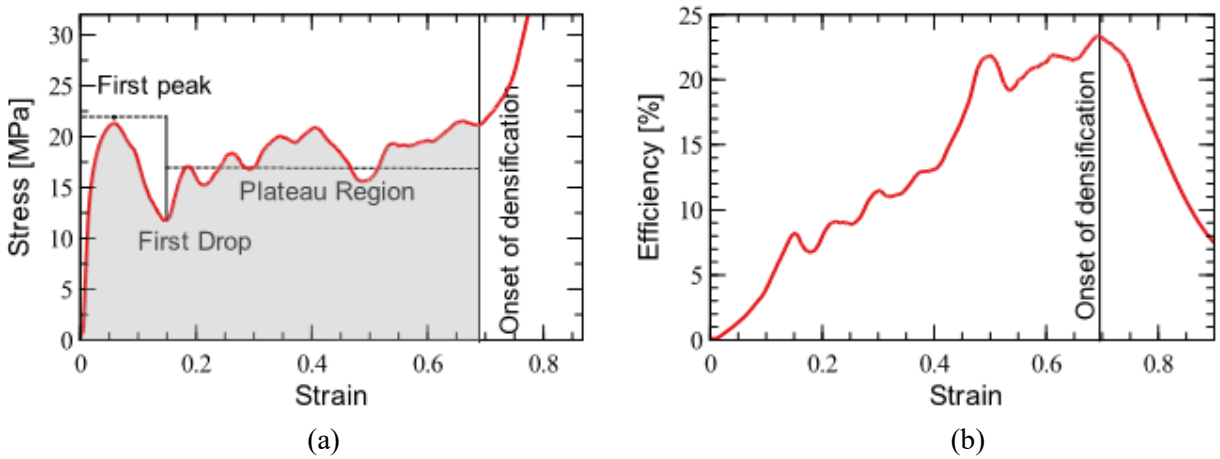

Figure 1. (a) A typical compression stress-strain response of a cellular material, showing the first peak, the plateau region, and the onset of densification, and (b) Energy efficiency graphed against displacement, with the peak used to identify the onset strain of densification (reproduced from [1] under CC BY 4.0 license)

Another challenge with designing optimal cellular materials is the modeling and simulation difficulties associated with performing large deformation studies with significant contact and sliding inherent in the process of generating the data needed to assess the materials' performance as an energy absorber. This is why the vast majority of publications in the energy absorption of cellular materials tend to be experimental in nature [4], [5], [6]. This is an acceptable approach when the variable being evaluated is topology, relative density and/or composition – but as shown in Figure 2, these are only three of the four approaches to manipulating cellular material geometry. A final approach is to use a field to influence one or more parameters within a cellular material, which as a result can now vary across space. This raises two questions (for now): why would one expect a "field driven" approach to be useful for energy absorption? And what kinds of fields could one apply to achieve these hoped for improvements?

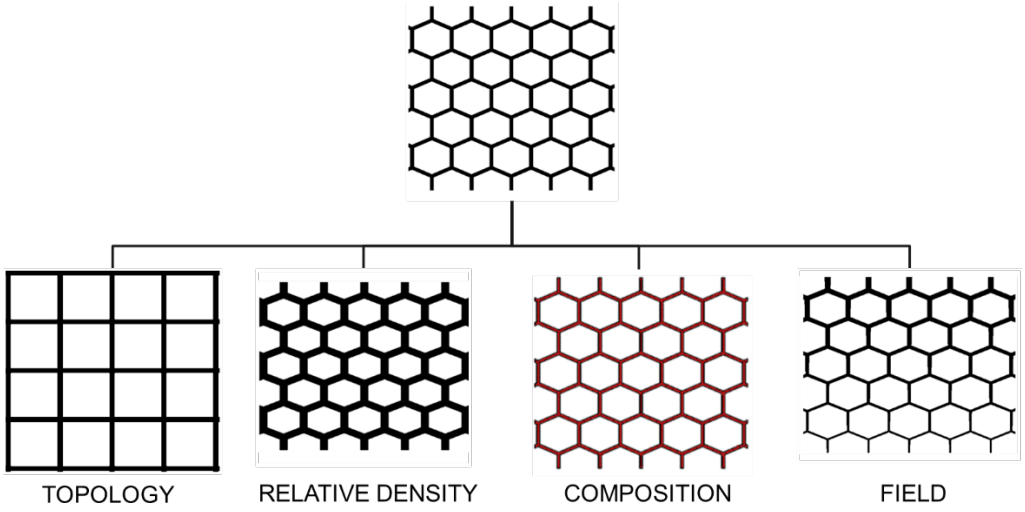

Figure 2. Four approaches to modulate the energy absorption of cellular materials: change topology, tune relative density, modify composition, and the focus of this work, modify cell parameters using a simulation generated field

The argument for field driven design of cellular materials to improve their energy absorption capabilities can be made on a purely empirical level: energy absorbers in engineering and in nature are very often stochastic in nature, with variable cell shapes and member thicknesses [7], [8]. The former is best represented in open cell foams, the latter by the structures in the beak of the toucan, to cite a few of many such examples [9]. With regard to the nature of fields, this work proposes a classification, categorizing all fields at the highest level as either rational or stochastic fields, as shown in Figure 3. The rational design method is typically used in metamaterial design to obtain desired properties by changing either material distribution or changing architecture locally. Crucially, rational design is based on a mathematical formulation or derived from simulation [10], and they may be thus further divided into analytical and simulation-driven fields. Analytical functions such as gradients define the former, whereas simulation-driven fields are obtained from numerical simulation of an initial design leveraging the solution output, for example, plastic energy density. Any scalar parameter from the output database of the simulation based on the objective can be used to influence design. In contrast to rational fields, stochastic fields are generated randomly – there are several approaches to achieve this [11], in this work they are categorized as simplex noise and cellular noise fields, which will be discussed later in more detail.

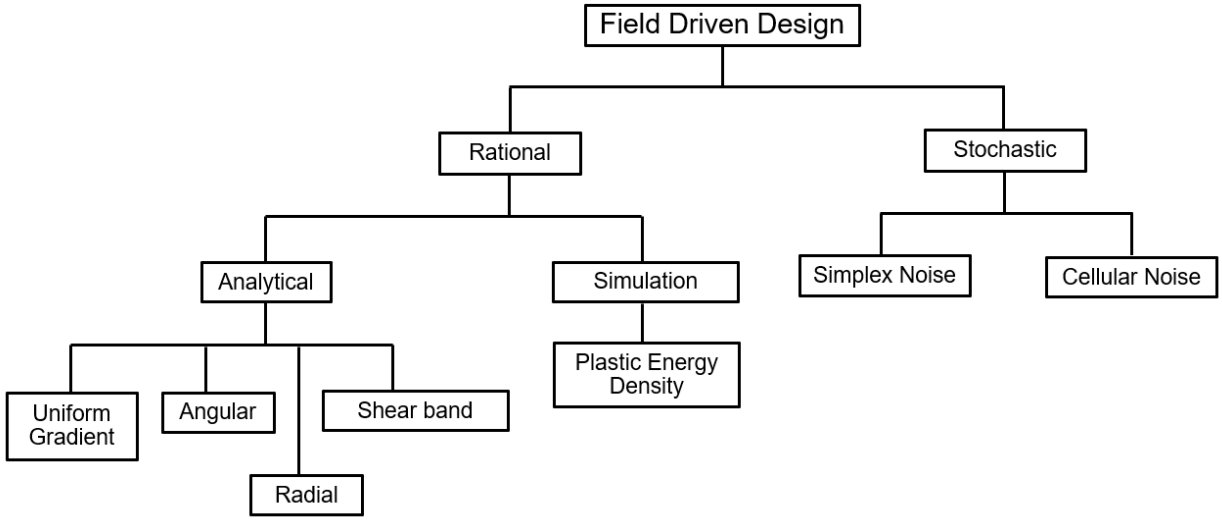

Figure 3. A proposed classification of the kinds of fields that may be leveraged for field driven design

With regard to fields derived from simulation, it is useful to identify the numerical challenges associated with this approach when attempting to design cellular materials for energy absorption. There are multiple ways to model cellular structures in FEA – a study on these approaches for Triply Periodic Minimal Surface (TPMS) geometries showed that while modeling these as shell elements improves computational efficiency, its applicability is limited to thin structures [12]. Solid elements can model structures of varying thickness but is computationally inefficient. All these limitations are exacerbated in the context of energy absorption, where (i) the entire structure needs to be modeled, thus ruling out the use of symmetry to simplify the problem, and (ii) the topology experiences large deformation which is vital to the estimation of the absorbed energy.

This work seeks to do the following: (i) develop and validate a modeling method for large deformation of TPMS geometries with variable thickness, (ii) examine the effects of using each of the fields in Figure 3, and (iii) identify promising strategies and opportunities for further

development of the field-driven design approach to the design of cellular materials for energy absorption. The scope of this work is limited to the Schwarz-P (Primitive) TPMS geometry [13], primarily because prior work had shown that it is susceptible to significant undulations in the plateau region [1] and thus had the highest potential for improving its energy absorption by modulating these undulations. The next section details the setup of the finite element (FE) model for this study, including its validation using experimental testing. The next section details the approach taken to enable variable thickness modeling, which is a precursor to enabling analysis of the field-driven design. This is followed by the simulation results for the different fields evaluated in this study. The work concludes with a discussion of the implications of this work.

Model Setup and Validation

Analytical fields can be applied directly to a design (covered later), but for simulation-derived field driven designs, one needs to have a valid, accurate and efficient modeling approach that generates pointwise information that can be applied to the design. This section deals with setting up an FE model that seeks to do just this. Once a design is modified by the field however, it needs a simulation technique capable of validating the performance of that design – this is treated separately in the next section.

As discussed previously, there are various approaches to modeling a TPMS geometry for mechanical analysis using the FE method. This work chose shell elements as the approach due to its computational efficiency – a crucial factor when conducting large deformation analyses of full-scale cellular materials. The mid surface of the quarter TPMS Schwarz Primitive structure was extracted and meshed in Hypermesh® Software (version 13.0). The quarter surface was meshed with four-node shell elements (S4). The nodes on the edges were checked for accuracy. A small node position error can lead to a significant deviation from the actual design due to arraying. The elements in the quarter section were copied and mirrored across the X, Y, and Z axis, respectively. As shown in Figure 4a, the complete unit cell was obtained by the abovementioned process, with 3696 nodes and 3661 elements in the unit cell model. For the Schwarz-P design shown here, the mirror operation works to populate a cellular structure as the geometry is symmetric across three axes.

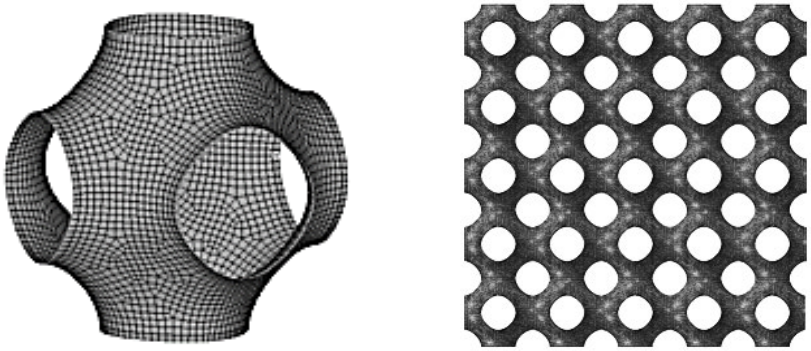

(a) (b)

Figure 4. (a) Schwarz-P unit cell meshed with shell elements, and (b) front view of the full 3D model of the Schwarz-P structure consisting of 125 unit cells, meshed with shell elements.

Once the unit cell was modeled, the quality of elements was checked (with regard to warpage, skewness etc.) against recommended values for reliable output with shell elements [14]. The generated mesh met all the criteria for excellent quality mesh. The elements were then copied and arrayed to generate a final design, shown in Figure 4b, having 125 unit cells and matched to a planned experimental test (discussed later). The full mesh consisted of 4,61,980 nodes and 4,57,680 elements.

To obtain a material model for implementing into the FE model, tensile test specimens were designed following the ASTM D638-14 standard [15] and fabricated using the Selective Laser Sintering (SLS) process on the EOS Formiga P110 out of Nylon-12 [16]. Prior work has shown that there is little effect of orientation on the modulus and tensile strength in SLS Nylon-12 specimens [17] – as a result all specimens were fabricated and evaluated only in the vertical (z) direction (along the build direction). Uniaxial tensile tests were conducted at a strain rate of 10^{-5} S^{-1} using a 250 kN Instron 5985 universal testing machine with a video extensometer (Figure 5a). To model Nylon-12 for this study, an isotropic elastic multilinear plastic material model was selected, which depends on two components. The elastic material definition requires two independent elastic constants: Young's modulus and Poisson's ratio. Young's modulus was calculated from experimental data using a MATLAB script. A Poisson's ratio value of 0.4 was established based on experiments carried out in the literature [18]. The plastic stress-plastic strain curve was obtained from the true stress-true strain data obtained experimentally, and is shown in Figure 5b. This is given as input in the form of a table in the Abaqus FE software. The Mises yield surface criterion was used to define isotropic yielding.

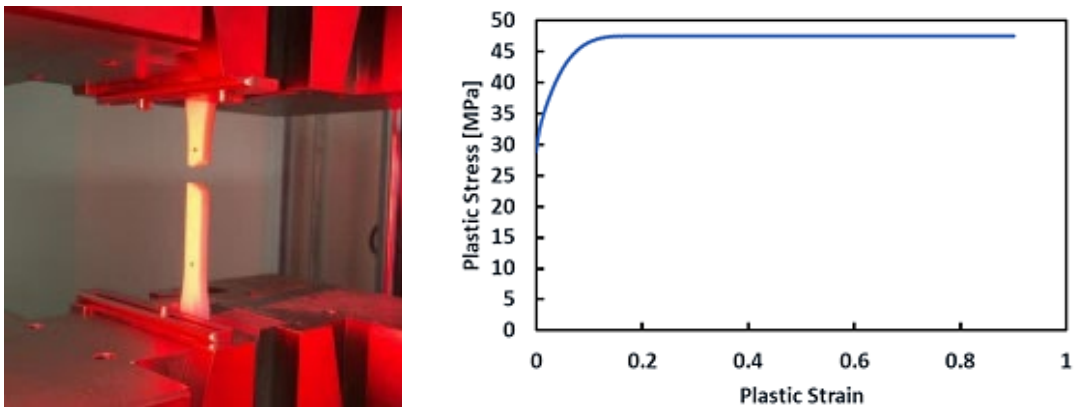

(a) (b)

Figure 5. (a) Tensile test specimen shortly after end of test, and (b) plastic stress-plastic strain curve used as an input to the FE model

A mesh convergence study was then conducted. For this, the model was setup to match the compressive loading conditions anticipated during the experimental study of the Schwarz-P structure for validation purposes (discussed later). These boundary conditions are shown in Figure 6a. The bottom face of the cell was in contact with another rigid plate at the bottom. The rigid bottom plate is constrained in all three directions. An infinitesimal displacement in the negative Z (downward) direction was applied at the top face of the unit cell using a rigid plate and the reaction force on the rigid top plate was recorded via reference point. The job was executed in the explicit solver of Abaqus, and the CPU time required to complete the job is recorded. The CPU time is directly proportional to the number of nodes in the model. Figure 5c shows the result of the mesh

convergence study, showing as expected that as the mesh becomes finer, the result obtained is less different from the prior mesh, but the number of elements is higher, resulting in higher simulation time. The reduction of mesh size from 0.4 mm to 0.3 mm resulted in a 0.72% decrease in the resultant force and a 34% increase in the simulation time. On further refinement of mesh size to 0.2 mm, the resultant force was reduced by 0.19%, and runtime was increased by 90%. This means the results obtained were only 0.19% different, but the required runtime was almost doubled. Hence the 0.3 mm element size was used in this study.

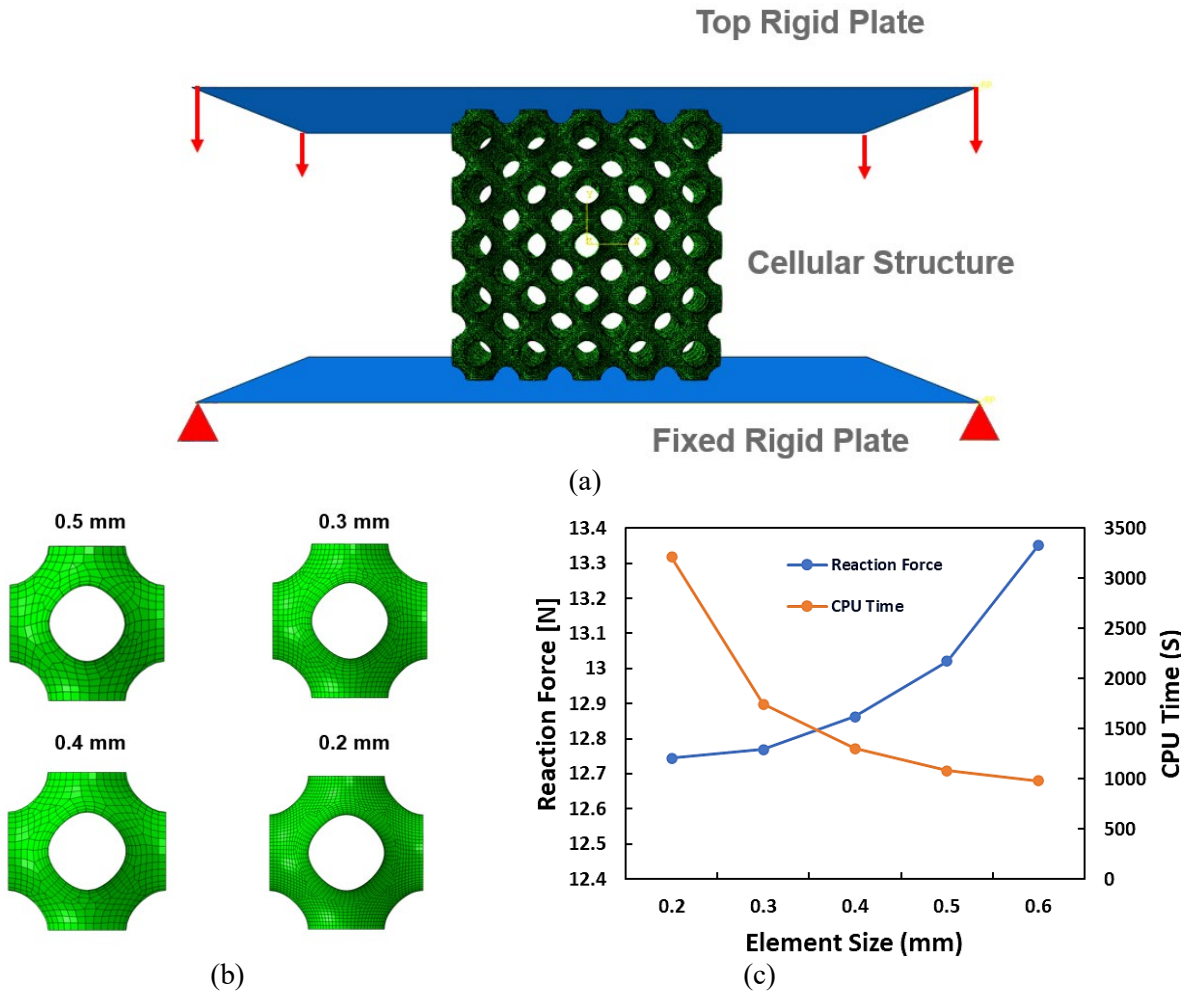

Figure 1. (a) Finite Element model of Schwarz-P structure with boundary conditions, (b) mesh sizes of shell elements used in the mesh convergence study, and (c) graph showing reaction force on the unit cell with blue curve and time required to run the complete simulation in seconds.

Having settled on a mesh size for this study, the next step is to run a full deformation analysis in Abaqus Explicit and set it up for experimental validation. For this, the rigid top plate was given a downward displacement of 30 mm over a period of 750 seconds, approximating to a strain rate of 0.001 per second for a 40 mm high cellular structure. This loading condition was selected to match the actual testing condition of the cellular structure performed experimentally. Semi-automatic mass scaling was used to keep the simulation time in check. A target time increment of 0.005 seconds was given. A homogeneous shell section was assigned to the cellular structure with five integration points across the thickness of the shell. Simpson's 5-point integration rule was used

across the thickness. The simulation was started and was found to be stable through the end of the test. The Von Mises stress contours obtained from the test are shown in Figure 7, with results plotted to a compression displacement of 27 mm (over a 40 mm initial height). After the first collapse of the cells, the walls of the cellular structure come in contact, and an explicit general contact was defined to account for the contact between the rigid plate and cellular block as well as self-contact of the cellular structure.

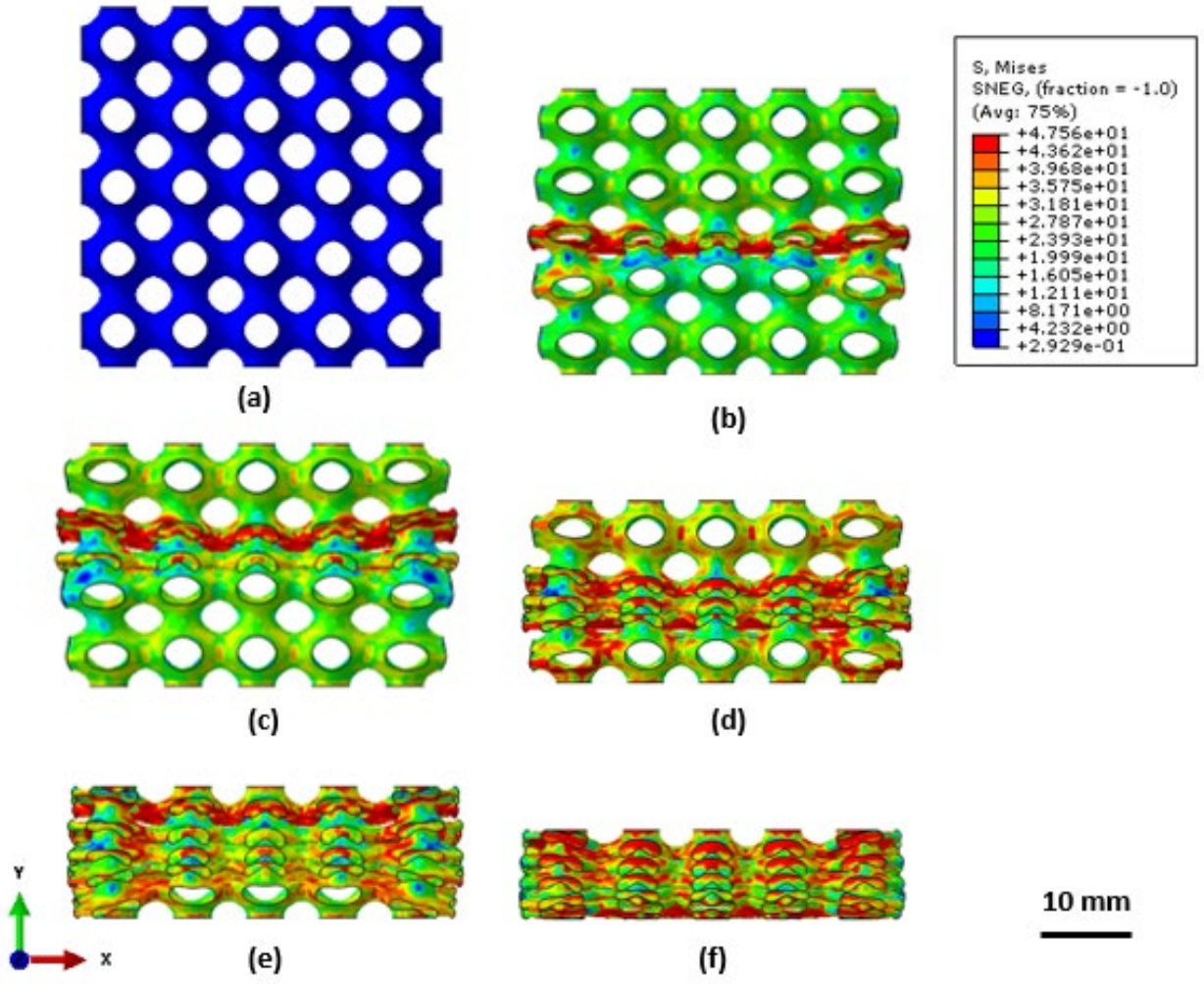

Figure 7. Deformation pattern and Von mises stress contours (Abaqus Explicit) in the Schwarz-Primitive cellular structure at (a) 0 mm, (b) 6 mm, (c) 12 mm, (d) 16.5 mm, (e) 21 mm, and (f) 27 mm displacement.

A final step prior to experimental validation is to verify the energy balance, as is typically conducted for explicit solutions. As semi-automatic mass scaling was used for the simulation, it was critical to check the mass scaling work in the complete simulation. External work, internal energy, artificial energy, and mass scaling work are plotted against simulation time in Figure 8. The ratio of external work done to internal energy at the end of the simulation was found to be 0.98, indicating that 98% of external work was converted into internal energy, and 2% of the energy was required for mass scaling work and added as artificial energy to compensate for overclosures in the contact. The artificial energy in the simulation should generally be less than

5% [85]. In this work, the artificial energy added due to mass scaling was found to be 2% - hence, it was concluded that the mass scaling assumptions used were valid.

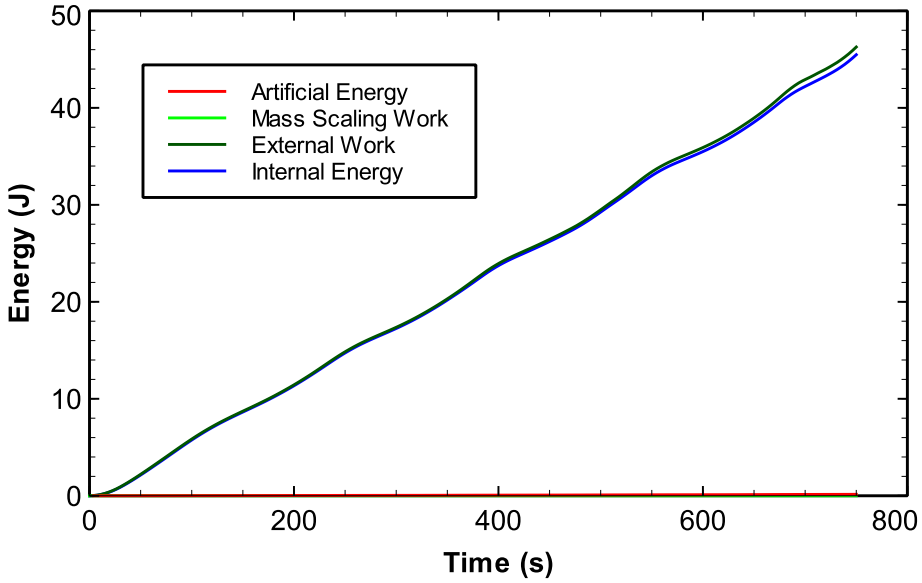

Figure 8. Energy balance for the Schwarz-P uniaxial compression simulation showing low artificial energy and low mass scaling work as compared to external work.

The next step was to validate the simulation against experimental data. For this, the same SLS process used to derive the material model was used to fabricate Schwarz-P structures with the same design as the one used in the simulation – for this experiment, a thickness of 0.4 mm was selected. Three identical specimens were tested under compression at an effective strain rate of 10^{-3} s^{-1}. The force displacement results from these tests are plotted against those obtained from the simulation and are shown together in Figure 9a – while the initial response is remarkably close to experimental data, it is clear that as deformation increases, the simulation overestimates the distance between the peaks and valleys in the undulations, eventually estimating an onset strain of densification that is about 7.5% higher than that observed experimentally. To improve the agreement between simulation and experimental results, continuum shell elements were considered at this stage. While conventional shell elements have been used with great promise when modeling sheet metal parts with uniform thickness and low aspect ratio, but at large strains, errors accumulate especially in geometries like the one in this study, which is not truly a thin, high-aspect ratio structure. Continuum shell elements have some advantages over conventional shell elements – much like solid elements, they discretize the three-dimensional body as opposed to conventional shell elements, which only discretize the reference surface. For continuum shell elements, the thickness is determined from the nodal position. Continuum shell elements have only a translational degree of freedom and can be stacked and hence used with greater accuracy for higher aspect ratio geometries. The thickness direction, element normal, and stacking direction in continuum shell elements are determined by nodal connectivity. Using these elements, results were improved, as shown in Figure 9b, with greater agreement between simulation and experimental results. Figure 9c shows the deformation patterns in the experiment and simulation, also showing good agreement, including correctly identifying the sequence of cell collapse.

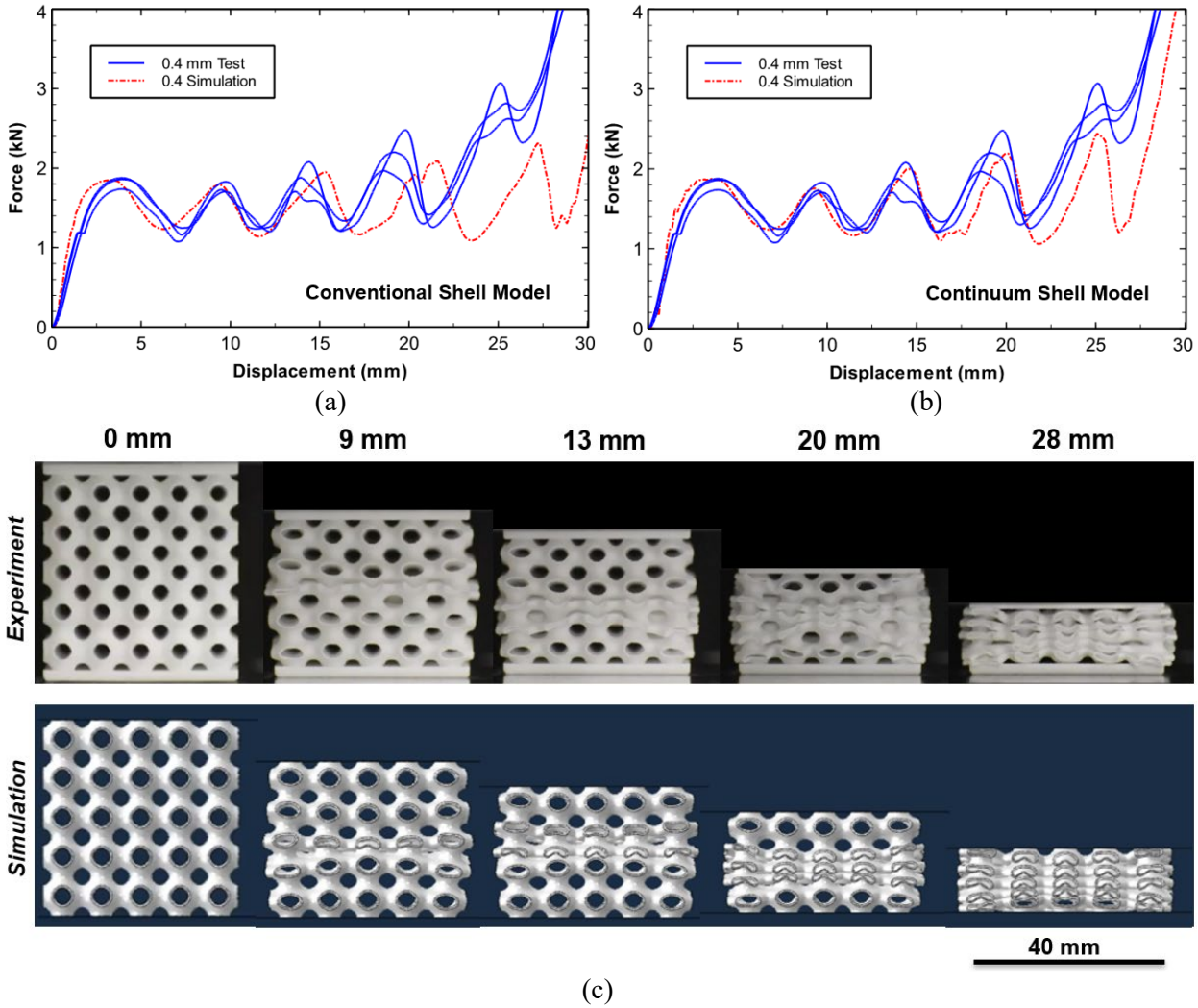

Figure 9. Comparison of simulation and experimental results for 0.4mm thick Schwarz-P cellular structure under uniaxial compression loading: (a) using conventional shell elements, (b) with continuum shell elements, and (c) comparison of deformation patterns showing good agreement.

Conventional shell elements assume a constant thickness, but the need in this work is for an element that can permit variable thickness, and continuity between elements. While previous work has looked at enabling variable thickness TPMS structures in Computer Aided Design (CAD) [19], those efforts have not embedded the capability in physics-based simulation, a key requirement to transfer a simulation driven field onto a design structure, but also for taking a field not derived from simulation and applying it to geometry for subsequent analysis using explicit FE. To implement variable thickness, a mid-surface is introduced into the element, as shown in Figure 10a. To generate uniform thickness continuum shell elements, the mid-surface is offset by half the thickness in both directions, but for the variable thickness shell elements, each node must be offset by a different value. Four elements share a node, and nodal connectivity must be retained. It is impractical to do this procedure manually for the entire structure with over a million elements. As a result, an Abaqus script was developed to generate a mesh with variable thickness continuum shell elements. The flowchart of the script is given in Figure 10b. The input required for the script is the element number and thickness associated with each element. The script groups the elements

according to the associated thickness. After the grouping, the elements in each group are offset by the thickness associated with the group. This approach is more efficient than offsetting each element individually due to the number of elements involved in the operation. Each node shared by four elements generates four new nodes. These four nodes are then interpolated to the midpoint to generate the connected mesh. This methodology thus successfully develops variable thickness continuum shell element models of the Schwarz-Primitive structures. To the best of the authors' knowledge, this is first attempt to model TPMS structures with continuum shell elements and further, enable variable thicknesses within these models for analysis and design.

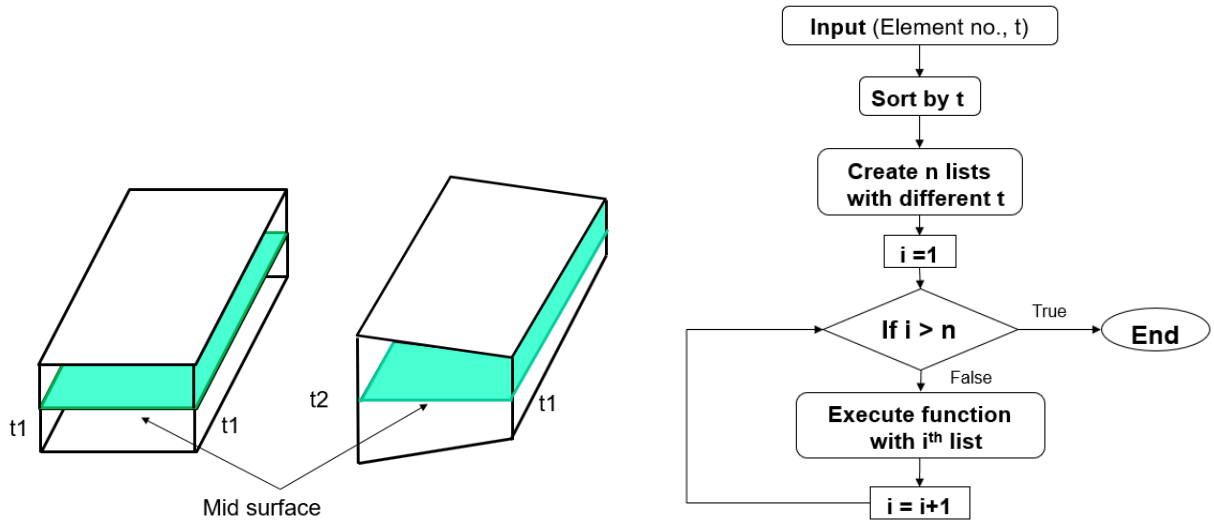

(a) (b)

Figure 2 (a) Difference between offset function for uniform thickness and variable thickness continuum shell elements, and (b) flowchart for Abaqus script to generate variable thickness continuum shell elements.

Field Driven Design: Implementation and Results

The discussion so far has involved establishing an FE model that is capable of generating fields for simulation driven design, and also for running simulations on variable thickness field-driven designed cellular materials. However, this is just one part of the larger workflow needed to enable field-driven design. While there are likely many different approaches towards achieving the stated objectives of this work, the approach taken here is shown in Figure 11. The design process begins with a primitive design, setup in the nTopology implicit design software [20]. Depending on the type of field desired, the workflow is different – for analytical or stochastic fields, the nTopology software is adequately able to represent and apply these to create structures with variable thicknesses. These are then exported to Abaqus with the previously mentioned script applied to generate a nodal cloud which is then exported to HyperMesh [21] for converting into a mesh for analysis, which is conducted in Abaqus Explicit. For simulation-driven designs, the field is generated via a simulation. As a result, the primitive design is directly exported to HyperMesh to generate a mesh for an FE analysis in Abaqus, which results in a simulation output file, which is then imported into nTopology and used as a scalar field to generate a variable thickness structure, and returned to the Abaqus-HyperMesh workflow as before. The rest of this section presents the results from each of these different fields – it begins with the simulation-driven design since the

results of this design were also additively manufactured and tested for validating the variable thickness modeling approach. This is followed by a discussion of the analytical and stochastic fields.

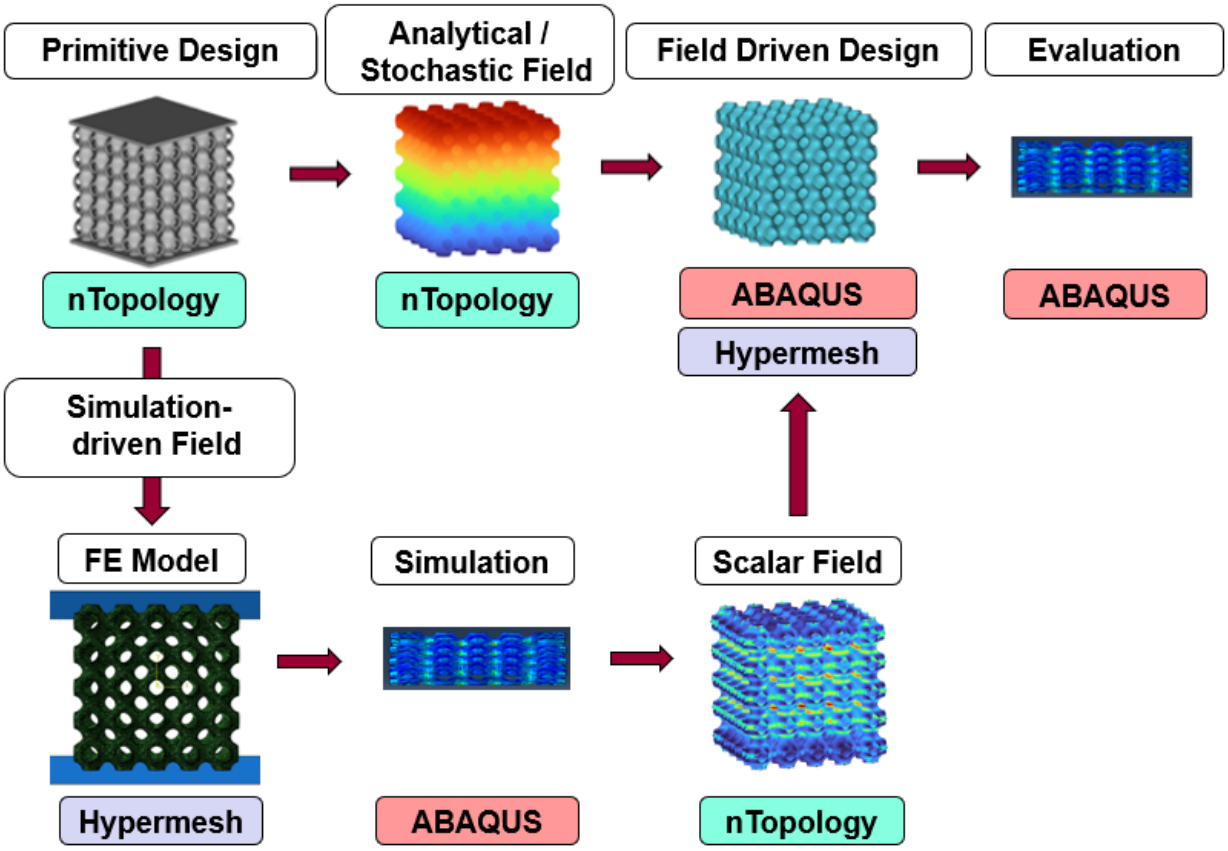

Figure 3 Design methodology for field driven design using analytical or stochastic fields, and simulation driven fields, leveraging different software platforms to accomplish all steps.

A. Simulation-driven Field

To apply simulation-driven design for the design of cellular materials for energy absorption, the following questions need to be addressed: (i) which field parameter should be chosen? (ii) what stage of the deformation should the field be extracted at? (iii) how should the field parameter influence local design parameters such as thickness and cell size? Each of these three questions is tackled in turn.

Since the key output measure of interest here is energy absorption, it follows that the parameter of most relevance is the one that tracks dissipation of external work. For the simulations run, as is expected, approximately 95% of the external work is converted into plastic energy, and only 5% of the work is recoverable elastic energy. Thus, it may be hypothesized that the *plastic energy density field* is the appropriate measure of choice and can be used to modify the thickness distribution of the cellular materials. As an example, the plastic energy density is shown for a compressed Schwarz-P structure in Figure 12 as well as mapped onto the undeformed structure, so its distribution can be seen. For the second question, the most appropriate stage of deformation

to extract the plastic energy density (PED) field was the onset strain of densification since this represents the accumulation of all useful dissipation that manifests in the estimated energy absorption of the cellular material. Subsequent plastic dissipation (i.e. beyond the onset strain of densification) is not relevant for a practical energy absorber.

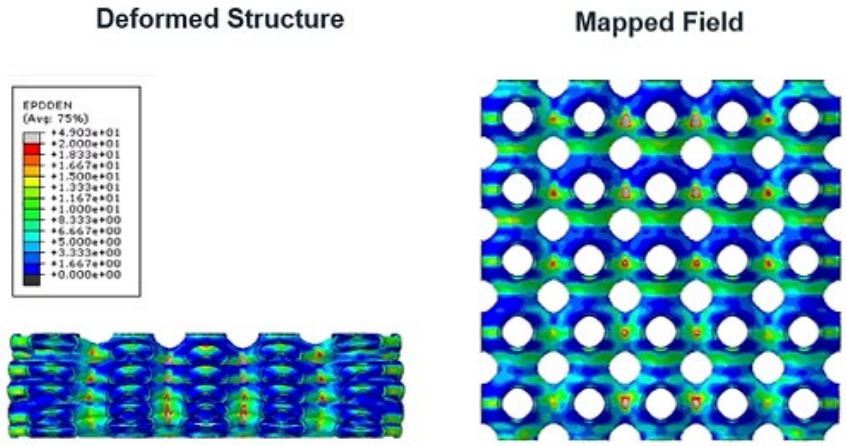

Figure 12. Deformed specimen and plastic energy density field mapped onto the undeformed structure

The final question – which seeks to identify the relationship between the plastic energy density field at the onset strain of densification and the resulting modification to local thickness - is a difficult one to answer using first principles alone. An additional complication is that changing thickness has the effect of changing the total mass (or relative density) of the redesigned structure. To address this latter concern, an approach was developed to distribute thickness in the modified structure in such a manner that the total mass of the structure was unchanged by less than 5% relative to the primitive design. The core idea behind this approach is to develop an empirical cumulative distribution function (ECDF) plot, shown in Figure 13a, that identifies all the nodes in the structure and their associated PED values in a single plot. As seen in this plot, 95% of the nodes experience a PED lower than 14.5 J/mm^3, the highest value is 54 J/mm^3 and 50% of the nodes have a PED less than 4.5 J/mm^3. Once the PED at onset strain of densification is known for each node, it must be leveraged to scale nodal thickness by a proportionate amount, based on a hypothesis that increasing thickness in nodes of high PED will result in better distribution of energy dissipation and therefore reduce undulations. Implementing this however raises two further questions: the range of thickness (maximum to minimum) and the scaling law that will be applied between these. For this work, five different ranges were selected (indicated A through E, Figure 13b), and linear mapping was used to scale thickness relative to PED in between these two, finding that the overall relative density did increase, but remained within 3% of the initial value. Changes in local thickness were confirmed visually, and are shown in Figure 13c for one example.

The “C” variant was exported as an STL file and additively manufactured and tested under compression using the same processes discussed previously and compared to a simulation result, showing reasonably good agreement for both the stress-strain response (Figure 14a) and the deformation pattern (Figure 14b) – going some length to validate the use of the continuum shell model for variable thickness designs. The main practical objective of this study was however, to asses if energy absorption can be enhanced with this approach – in particular, whether plateau undulations can be reduced.

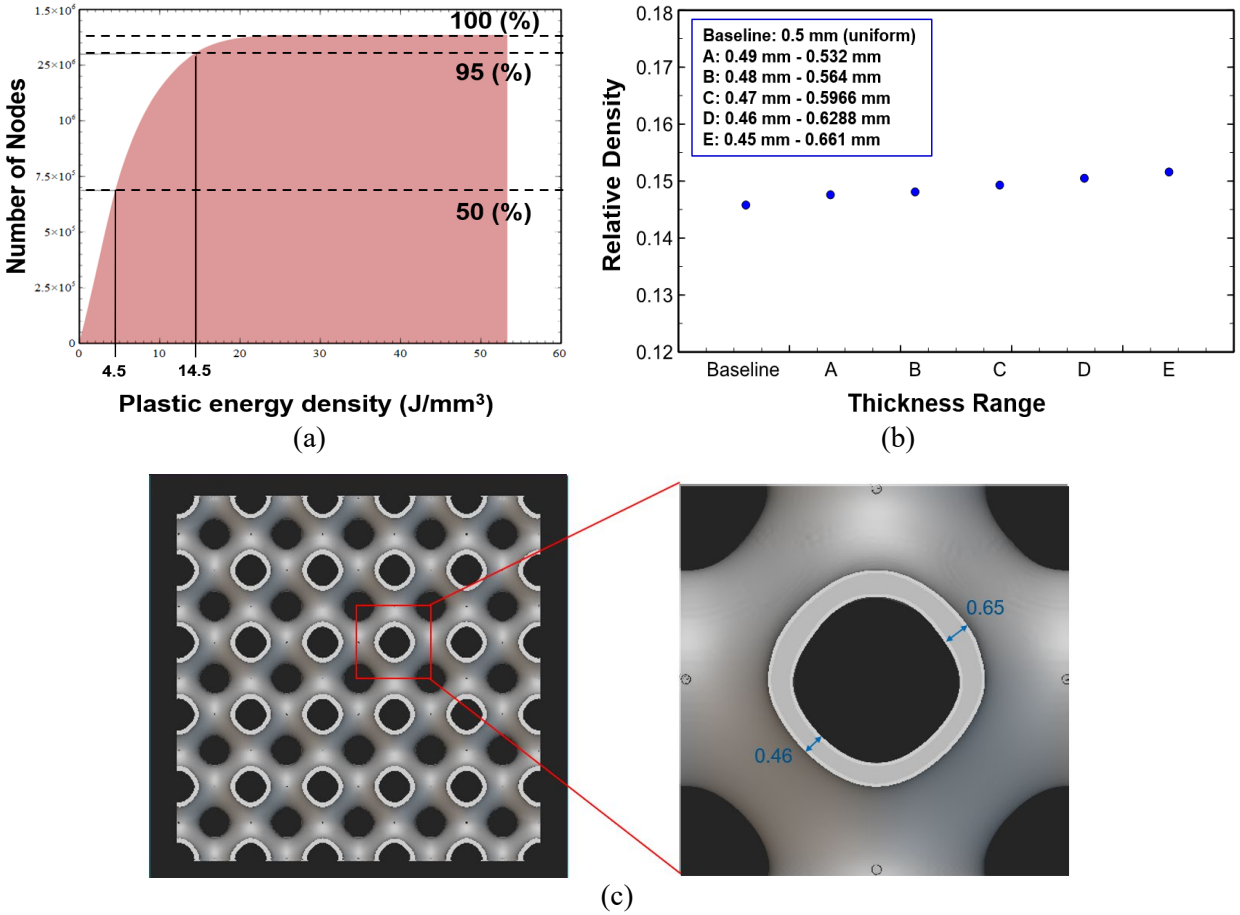

(a) (b)

(c)

Figure 13. (a) Empirical cumulative distribution function showing number of nodes and associated plastic energy density values at onset strain of densification, (b) relative density of simulation driven designs with variable thickness, and (c) confirmation of variable thickness in the resulting Schwarz-P structure

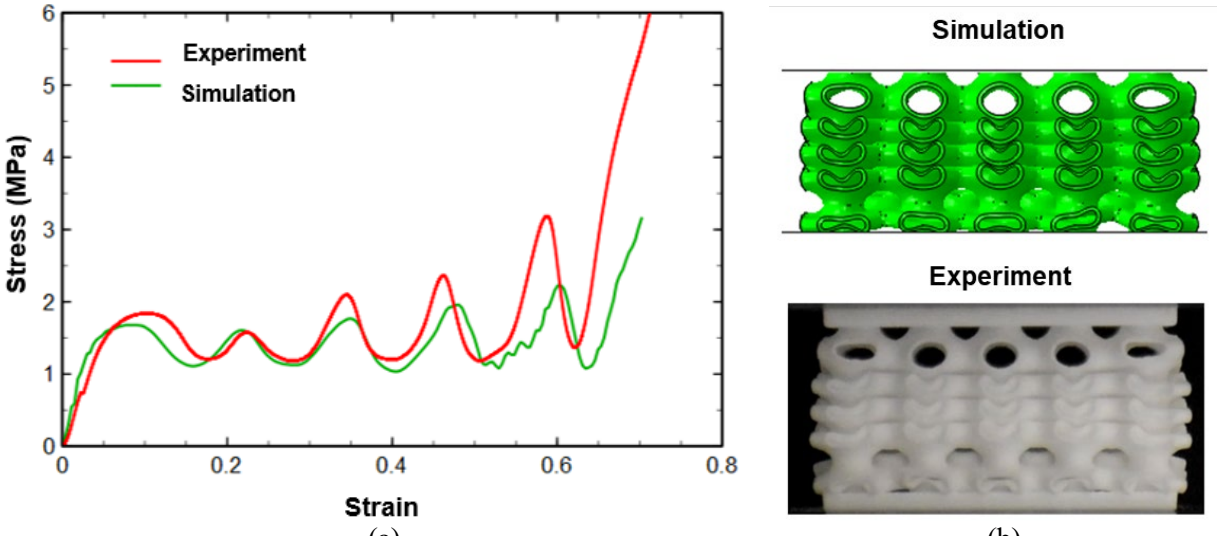

(a) (b)

Figure 14. (a) Comparison between experimental and simulation compression test results for a simulation field driven designed Schwarz-P structure, and (b) deformation patterns at the onset strain of densification

To assess if such a simulation-driven approach could reduce undulations in the plateau, all five variants were manufactured along with the baseline and tested under compression. Results are shown in Figure 15a, and clearly show, if anything, an increase in undulations in the plateau region. The reason for this is likely that thickening regions of high PED only exacerbated the layer-by-layer collapse of the Schwarz-P structure relative to the baseline, where the PED accumulation and subsequent cell collapse is more uniformly distributed – which is a key factor for fewer undulations in the stress plateau [22].

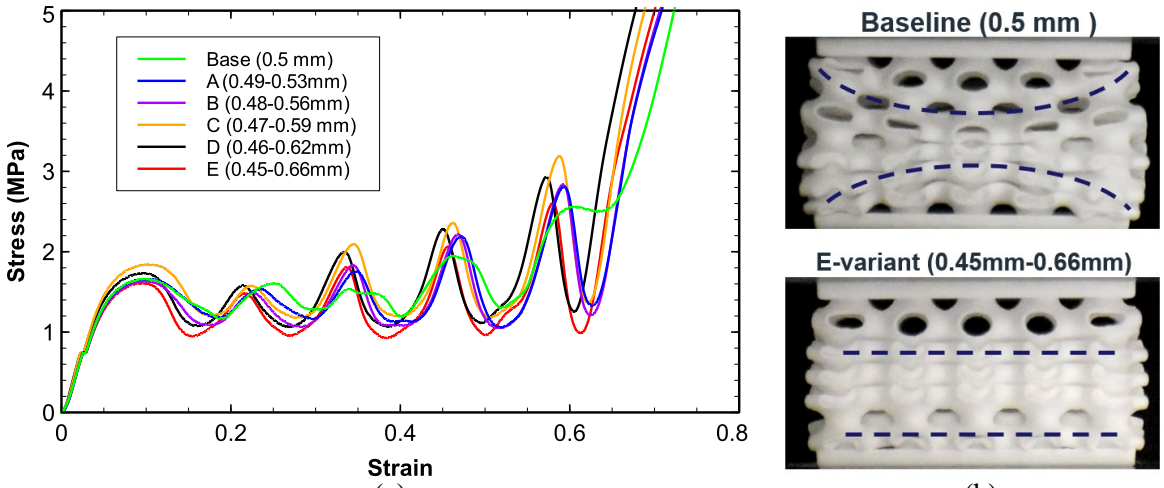

(a) (b)

Figure 15. (a) Experimental results from testing all five simulation-driven design variants relative to the baseline, and (b) deformation pattern at the onset strain of densification

B. Analytical Fields

Analytical fields are those that are prescribed mathematically – and unlike the previously discussed simulation-driven approaches benefit from a rationale that justifies their application. This work sought to demonstrate these fields in the framework developed – as a result, two different fields (linear gradient and failure band localization) were selected, with results reported below. More work needs to be done to optimize these fields for energy absorption.

B1. Linear Gradient

One of the more commonly studied fields in the literature is the linear gradient [23], where the parameter of interest (thickness of the wall, for example) is a function of Z-axis co-ordinate as given by the equation:

$$t = A + B * z \tag{1}$$

In the context of this work, t is the thickness of the wall, z indicates the Z co-ordinate of the point on the Schwarz-P mid surface, and A and B are constants that influence the minimum thickness at $z = 0$ (which specifies A), and the scaling factor that determines the strength of the gradient (B). For this exploration, an A value of 0.44, and a B value of 0.3 was chosen to keep the relative density of the structure the same as that of the baseline uniform thickness structure with 0.5 mm thickness – the resulting structure is shown with thickness contours in Figure 16a. The simulation results of the compression of the graded structure is shown relative to the baseline in Figure 16b and indicates that the undulations do reduce somewhat, especially after the first drop in stress. This may be

attributable to the programmed sequence of collapse from the thinner walls at the bottom to the thickest at the top, with the undulations gradually reducing as the walls get thicker and the stress drops are not as sharp. On analysis, the Specific Energy Absorption (SEA) of the graded structure was found to be 10% higher than the uniform thickness structure.

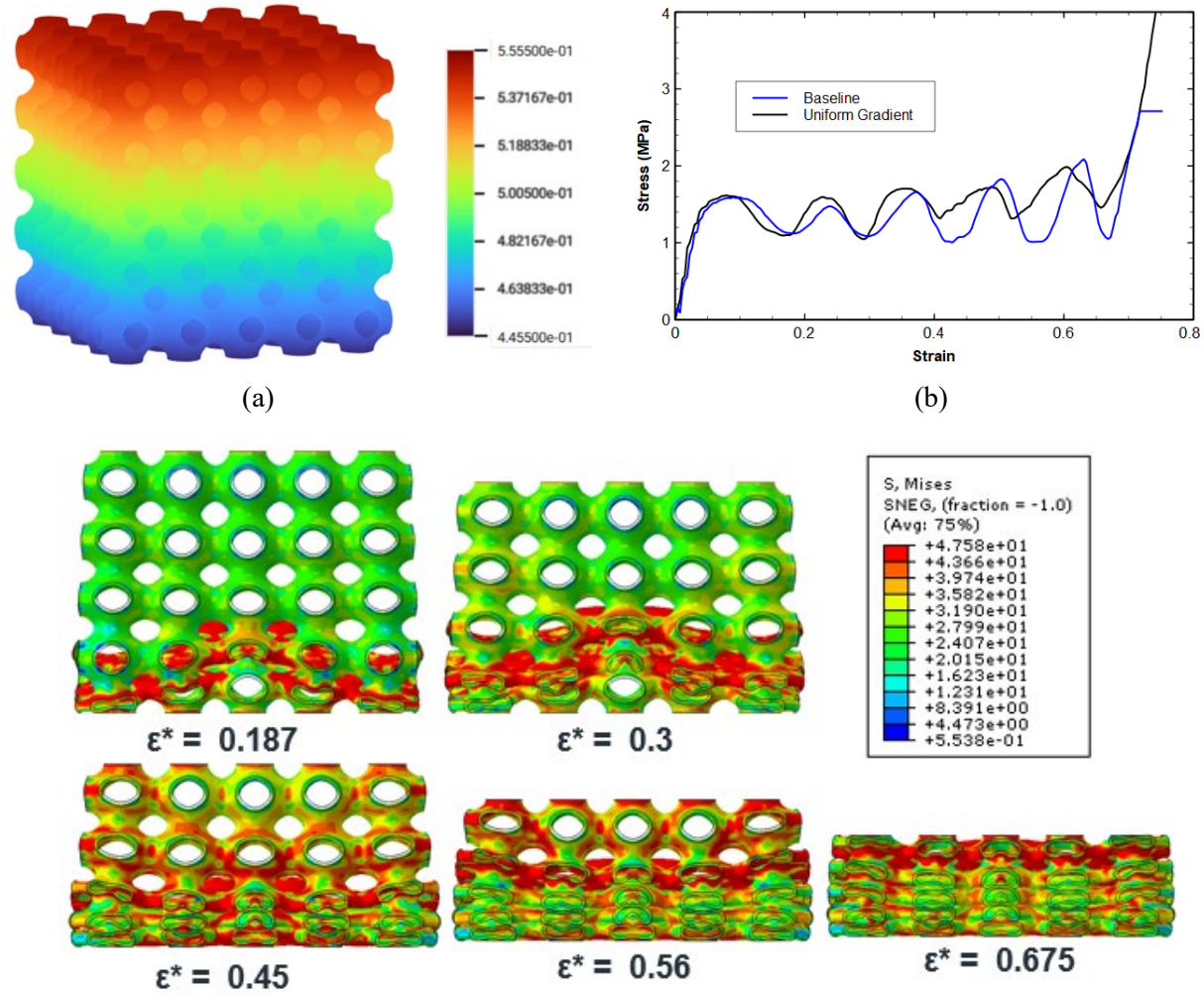

Figure 16. (a) Linear gradient of wall thickness varying from 0.44 mm to 0.56 mm indicated by contours representing thickness values, (b) simulation results comparing compression responses of the uniform gradient and the baseline with no gradient, and (c) simulated collapse sequence for uniform gradient structure

Further improvements to the undulations of the plateau stress require an examination of its underlying causes. Each dip in the stress plateau corresponds to a sympathetic collapse of multiple cells – thus it is reasonable to hypothesize that a field that takes cell collapse into consideration is likely to improve performance by reducing undulations. The uniform field, while an improvement over the baseline, does not incorporate any information from the physics of collapse. The simulation driven design, while being a far more physically relevant approach, is challenging to meaningfully implement when the field continuously evolves during the deformation process itself. As a result, the next field that was examined was one designed with the intent of driving the localization of cell collapse in a favorable orientation.

B2. Failure Band Localization

Localization of failure in cellular materials is often a driver of undulations in the stress plateau. Row-wise collapses of the kind seen for the Schwarz-P structure shown so far in particular causes stress dips and rises as each plane of cells simultaneously collapse. When cells collapse long a diagonal however, as seen in prior work shown in Figure 17, undulations are reduced [1]. This work thus sought to convert the row-wise collapse in the baseline, constant thickness design into a diagonal failure band by introducing a thickness gradient with the lowest thickness along the diagonal to test the hypothesis that this would reduce undulations by delocalizing cell collapse.

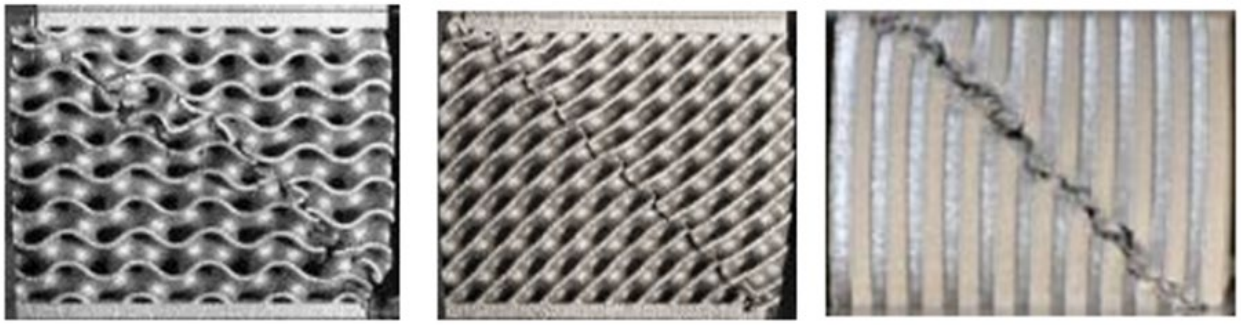

(a) (b) (c)

Figure 17. Examples of failure band localization along the diagonal in three different cellular materials: (a) gyroid, (b) diamond, and (c) honeycomb (reproduced from [1] under CC BY 4.0 license)

To evaluate if this would be the case, a baseline Schwarz-P geometry with a uniform 0.5mm thickness was modified by introducing a linear thickness gradient – but instead of changing the thickness along the direction of compression as was done previously, the thickness varied from the 45^{o} diagonal plane, going outwards, as shown in Figure 18a. The thickness was varied from 0.43 mm to 0.55 mm – as before, this range was selected to result in a relative density that was within 5% of the relative density of the baseline design. The FEA model was generated, and a uniaxial compression simulation was carried out to obtain a stress-strain curve for the variable thickness structure. Figure 18b shows the comparison of the stress-strain curves with the solid lines, suggesting significant improvement in the shear band field with regard to reducing undulations. An examination of the number of cells that were in a collapsed state (defined as the point where the cell had experienced greater than 50% deformation relative to its initial state) at any given global strain during the compression event showed that the hypothesis that a shear band field would make the collapse sequence more uniform by delocalization of strain accumulation was validated, confirming previously reported work with stochastic TPMS geometries [22]. The deformation patterns and von Mises stress contours in Figure 18c clearly indicate a preference for the failure band – which is a departure from the row-wise collapse seen in the primitive structure (Figure 7). To quantify the reduction in undulations, a nondimensional measure first proposed by [24] called the Undulation of the Load-carrying Capacity (ULC) can be used. ULC tends to correlate inversely with energy efficiency, with an ideal energy absorber having a ULC value of 0. The estimated ULC of the failure band field is 0.108 against 0.2 for the baseline, which represents a remarkable 50% reduction in ULC. Thus the use of a failure band field is promising to drive collapse along certain preferable directions to improve the cellular material's energy absorption characteristics.

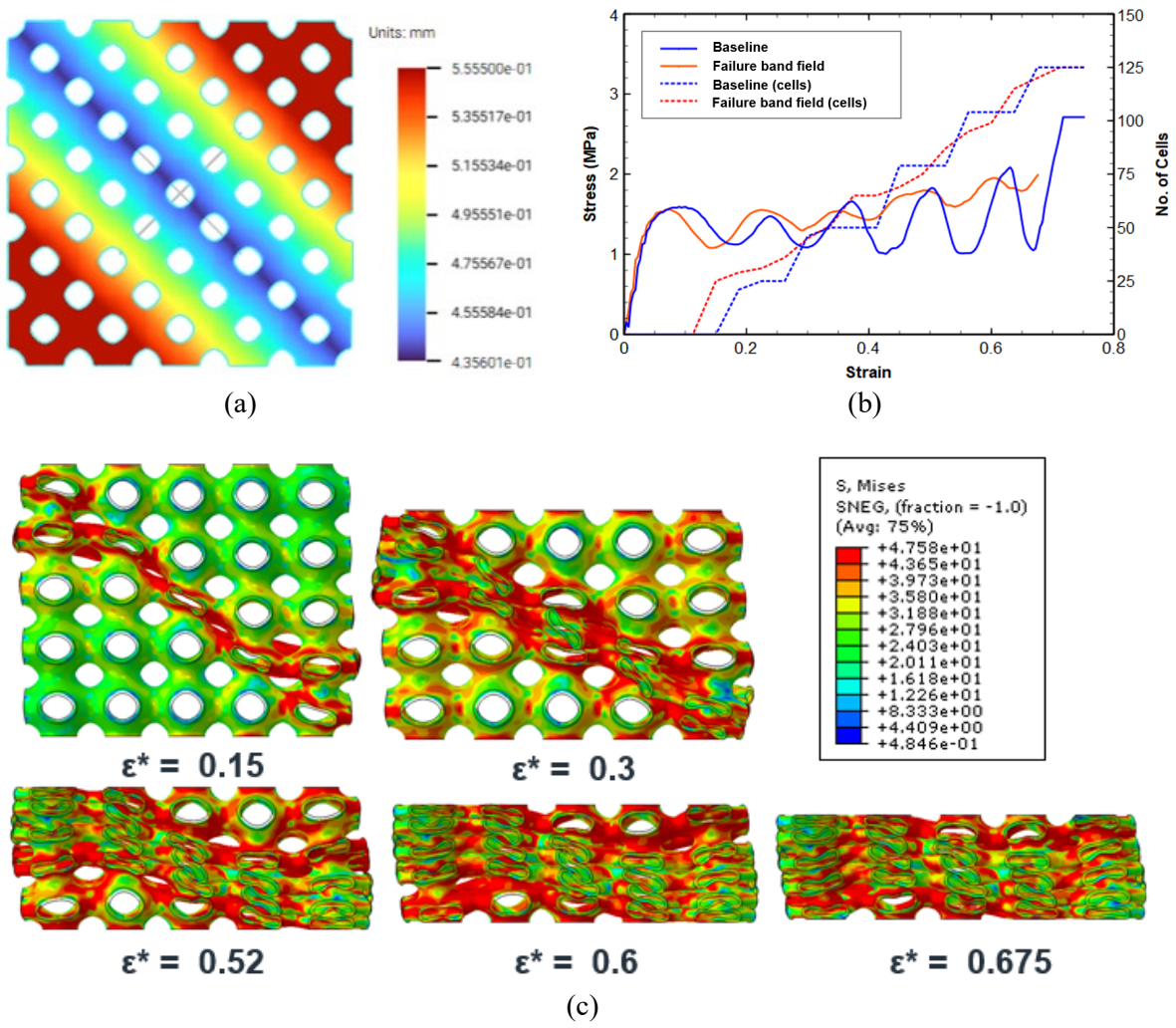

Figure 18. (a) Failure band field applied to baseline design, (b) compression stress-strain response of the primitive and failure band field designs along with the cumulative count of the number of cells that collapsed at that point, and (c) deformation patterns of the failure band field, clearly showing preference for collapse along the diagonal

C. Stochastic Fields

As opposed to rational fields, in stochastic fields, any point in space can have a random value of thickness based on its coordinates. The argument for using stochastic fields is that the random variation in the structure's thickness causes each cell to possess a unique stiffness, causing significantly improved delocalization under uniaxial compression. It is hypothesized therefore, that this will result in an even smoother plateau and high SEA for the structure as a whole. To test this hypothesis, two stochastic fields available in the nTopology software were used for convenience for this empirical study: simplex noise and cellular noise [25].

C1. Simplex noise field

A simplex algorithm uses a simplex shape to discretize the domain [26]. For example, to discretize the 2D domain, equilateral triangles are used, forming a tessellated grid. Each pixel is located in this grid, and gradients are associated with the grid points. A dot product of the gradient

and distance vector gives the output value at each point. Simplex noise uses a radial attenuation function to weigh each point - hence, no interpolation is required, generating high-quality noise [27]. Figure 19a shows the thickness distribution in the Schwarz-P structure generated using a simplex noise field. Once again, the thickness was specified to vary from 0.4 to 0.55 mm to keep relative density constant. The stress-strain response, and the cumulative cell collapse count graph in Figure 19b shows a slight reduction in undulations and delocalization of cell collapses – though not as significant as with the failure band field discussed previously. In fact, the simplex noise field generated a 38% reduction in ULC relative to the baseline. While the field had the effect of perturbing the geometry, the plane-wise collapse was still maintained for the most part, as seen in Figure 19c.

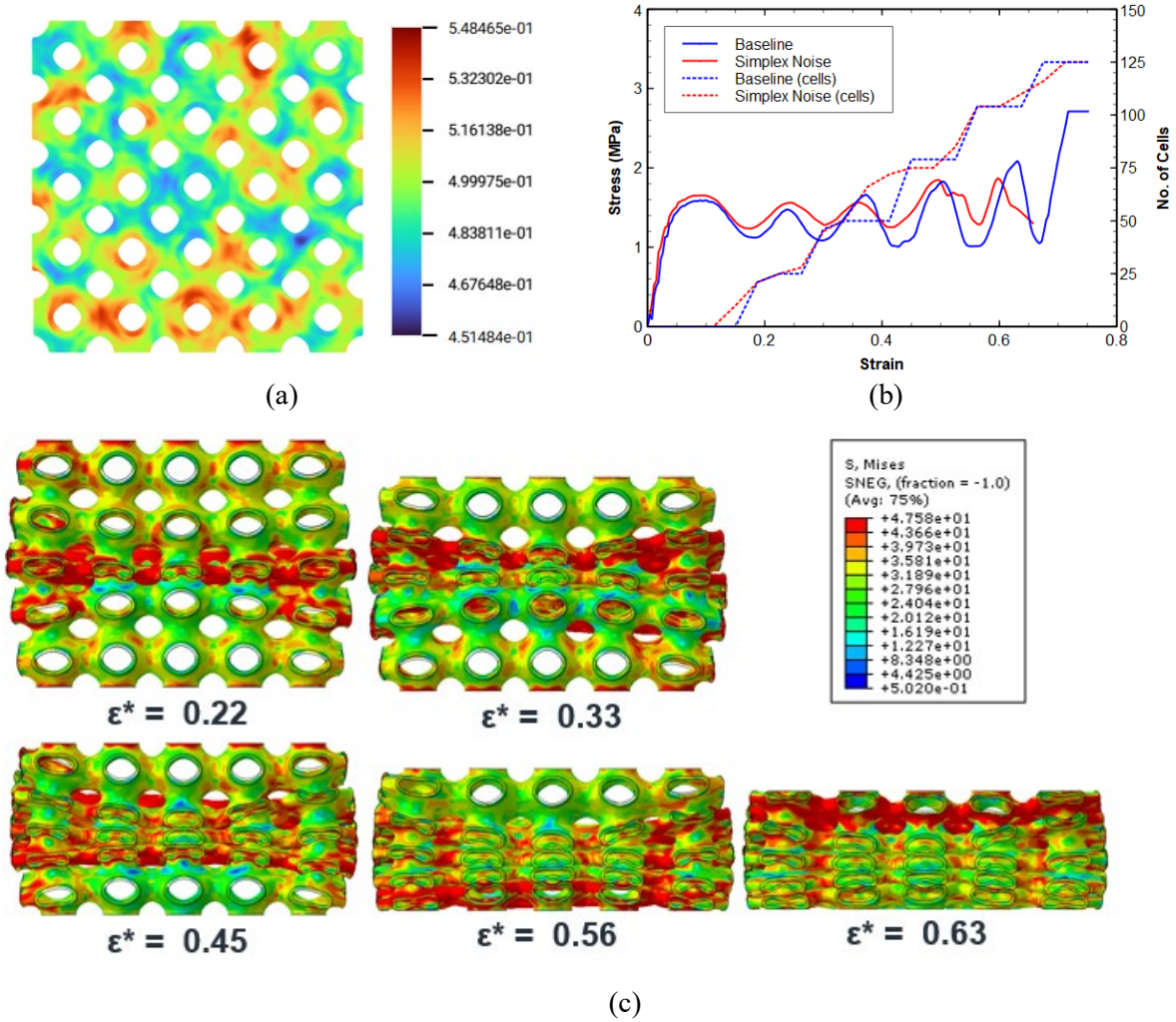

Figure 19. (a) Simplex noise field, (b) stress-strain and cumulative cell collapse count for baseline and simplex noise field cellular structure, and (c) deformation patterns, showing mostly row-plane wise collapse, with some non-uniformity evident.

C2. Cellular noise field

The final field studied in this work was the cellular noise field. In some sense, the cellular noise field may be said to combine the previous two fields into one. Without delving into the details, the first step in this process is the generation of random 3D Voronoi cells, with a grid of points defined

by the resulting nodes. As before, each cell contains pixels - the value of any given pixel is the distance of the nth closest node [27]. Based on the choice of n, the cellular noise is divided into Standard, Distance, Euclidean, and Manhattan subtypes - for the current study the distance field was used. The field generated in this study is shown in Figure 20a – it has the randomness similar to the simplex field, but also has the boundary of a Voronoi cell embedded in it that mimics the localization of the failure band. The lowest thickness values were specified along these Voronoi walls, with a randomized increase around it, corresponding to the pixel values, themselves influenced by the distance from the Voronoi nodes. The compression response of the cellular noise field is shown in Figure 20b along with the cumulative cell collapse graph, showing the lowest undulations of all the fields evaluated, and the smoothest cumulative cell collapse curve. The basis for the reduction in undulations is somewhat clarified in Figure 20c – the structure retains properties of failure band collapse formation combined with those of delocalization attributable to stochastic variation in thickness.

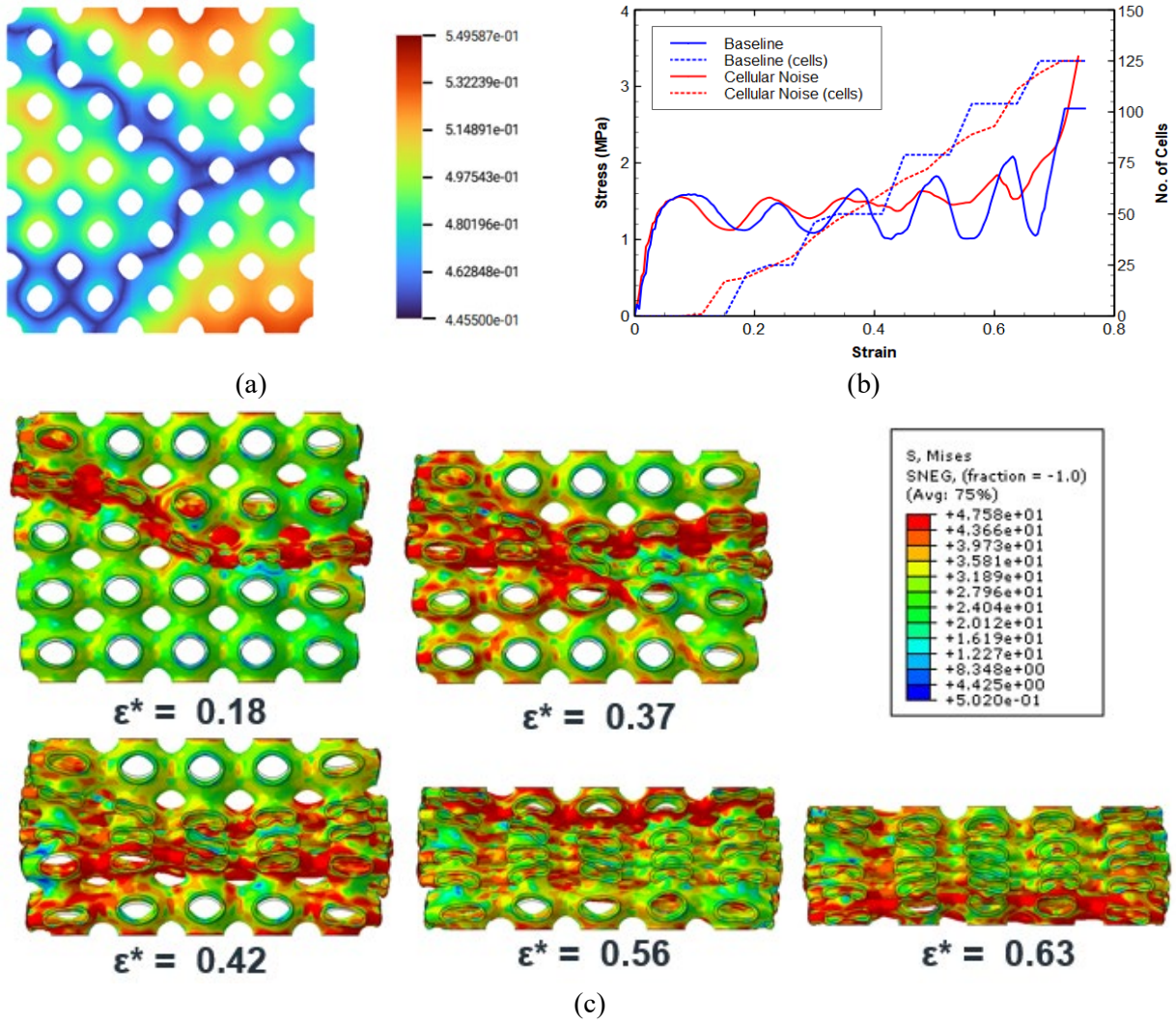

Figure 20. (a) Cellular noise field, (b) stress-strain and cumulative cell collapse count for baseline and cellular noise field cellular structure, and (c) deformation patterns and von Mises stress contours at various effective global strains.

Discussion

The primary purpose of this work was to develop and evaluate an approach for field driven design. While not the focus of the work, it is nonetheless worthwhile to discuss some of the key findings from the different fields themselves since they may provide direction for future research in developing specific fields for improving energy absorption performance. A total of four different fields were evaluated in this work: two rational, and two stochastic. With the caveat that these fields were not optimized in any significant way and were also constrained by the need to match the relative density of the baseline, the summary data associated with these specimens (all from simulation data) is shown in Table 1. This work suggests that the stochastic fields have the effect of significantly reducing the undulations (measured by ULC) in the stress plateau, though the failure band field maximized SEA. SEA is often normalized in the literature by the Maximum Transmitted Stress (MTS) since the designer of energy absorbers is often trying to maximize SEA for a given MTS target. Thus, the last column in Table 1 indicates this ratio and suggests that the simplex noise field is the best candidate at increasing SEA/MTS, with an 18% improvement over the baseline with a fixed thickness. The promise of stochastic fields indicated here recapitulates a well known empirical observation in stochastic foams, but the opportunity emerging from this work is to tune the stochasticity to achieve certain objectives better than the community has been able to do before.

Table 1. Comparison of energy absorption parameters for the field-driven designs studied in this work

Field	Onset Strain of Densification	Specific Energy Absorption (SEA) [J/g]	ULC	Maximum Transmitted Stress (MTS) [MPa]	SEA/MTS [m^3/kg]
Baseline (Fixed thickness)	0.66	57.15	0.18	2.09	3.03
Linear gradient	0.65	61.40	0.14	1.99	3.42
Failure band	0.65	62.61	0.13	1.95	3.56
Simplex noise	0.65	60.77	0.11	1.87	3.60
Cellular noise	0.63	57.69	0.10	1.84	3.47

Conclusions

This work has made the following contributions to the field of energy absorbing cellular materials:

- A method for field driven design of cellular materials for energy absorption was developed and demonstrated
- A continuum shell model was developed, implemented and validated for large deformation modeling and analysis of variable thickness Schwarz-P structures – the first such model that has been reported in the literature to the best of the authors knowledge.
- Four different fields – two rational and two stochastic were explored with promising results showed for all fields with regard to enhancing energy absorption behavior by lowering plateau undulations and/or increasing specific energy absorption

Future work will explore field optimization – simulation data may serve as powerful training data for machine learning (ML) approaches to cellular material design for energy absorption applications. The models in this work also did not use rate-dependent material models, which may further improve the agreement between simulation and experiment.

Generative AI Declaration

The authors declare that NO generative AI tools were used for any aspect of this work – from conception through execution, to writing and editing.

References

[1] M. Shinde, I. Ramirez-Chavez, D. Anderson, J. Fait, M. Jarrett, and D. Bhate, "Towards an Ideal Energy Absorber: Relating Failure Mechanisms and Energy Absorption Metrics in Additively Manufactured AlSi10Mg Cellular Structures under Quasistatic Compression," *Journal of Manufacturing and Materials Processing*, vol. 6, no. 6, p. 140, 2022, doi: 10.3390/jmmp6060140.

[2] M. Shinde, I. E. Ramirez-Chavez, A. Potts, and D. Bhate, "A Critical Assessment of the Onset Strain of Densification in the Evaluation of Energy Absorption for Additively Manufactured Cellular Materials," 2024. [Online]. Available: www.sciencedirect.com

[3] Y. Liu, T. A. Schaedler, A. J. Jacobsen, and X. Chen, "Quasi-static energy absorption of hollow microlattice structures," *Compos. B Eng.*, vol. 67, pp. 39–49, 2014, doi: 10.1016/j.compositesb.2014.06.024.

[4] H. Yin, W. Zhang, L. Zhu, F. Meng, J. Liu, and G. Wen, "Review on lattice structures for energy absorption properties," *Compos. Struct.*, vol. 304, no. P1, p. 116397, 2023, doi: 10.1016/j.compstruct.2022.116397.

[5] F. Xu, X. Zhang, and H. Zhang, "A review on functionally graded structures and materials for energy absorption," *Eng. Struct.*, vol. 171, no. May, pp. 309–325, 2018, doi: 10.1016/j.engstruct.2018.05.094.

[6] J. Zhang, G. Lu, and Z. You, "Large deformation and energy absorption of additively manufactured auxetic materials and structures : A review," *Composites Part B*, vol. 201, no. July, p. 108340, 2020, doi: 10.1016/j.compositesb.2020.108340.

[7] L. J. Gibson, M. F. Ashby, and B. A. Harley, *Cellular Materials in Nature and Medicine*, 1st ed. Cambridge University Press, 2010.

[8] L. Gibson and M. Ashby, *Cellular Solids: Structure and Properties*, 2nd ed. 1999.

[9] T. Mcnulty *et al.*, "A Framework for the Design of Biomimetic Cellular Materials for Additive Manufacturing," in *Solid Freeform Fabrication Symposium*, 2017, pp. 2188–2200.

[10] M. J. Mirzaali, R. Hedayati, P. Vena, L. Vergani, M. Strano, and A. A. Zadpoor, "Rational design of soft mechanical metamaterials: Independent tailoring of elastic properties with randomness," *Appl. Phys. Lett.*, vol. 111, no. 5, 2017, doi: 10.1063/1.4989441.

[11] I. E. Ramirez-Chavez, D. Anderson, R. Sharma, C. Lee, and D. Bhate, "A Classification of Aperiodic Architected Cellular Materials," *Designs (Basel).*, vol. 6, no. 4, Aug. 2022, doi: 10.3390/designs6040063.

[12] U. Simsek, A. Akbulut, C. E. Gayir, C. Basaran, and P. Sendur, "Modal characterization of additively manufactured TPMS structures: comparison between different modeling methods," *International Journal of Advanced Manufacturing Technology*, vol. 115, no. 3, pp. 657–674, 2021, doi: 10.1007/s00170-020-06174-0.

[13] L. Han and S. Che, "An Overview of Materials with Triply Periodic Minimal Surfaces and Related Geometry: From Biological Structures to Self-Assembled Systems," *Advanced Materials*, vol. 1705708, pp. 1–22, 2018, doi: 10.1002/adma.201705708.

[14] M. Smith, "ABAQUS/Standard User's Manual, Version 6.9 ," 2009, *Dassault Systèmes Simulia Corp , Providence, RI* .

[15] ASTM International, *Standard test method for tensile properties of plastics*. pp. 1–17. doi: 10.1520/D0638-14.1.

[16] A. Rajeev *et al.*, "Parametric optimization of corner radius in hexagonal honeycombs under in-plane compression," *J. Manuf. Process.*, vol. 79, pp. 35–46, Jul. 2022, doi: 10.1016/j.jmapro.2022.04.041.

[17] C. Majewski and N. Hopkinson, "Effect of section thickness and build orientation on tensile properties and material characteristics of laser sintered nylon-12 parts," *Rapid Prototyp. J.*, vol. 17, no. 3, pp. 176–180, 2011, doi: 10.1108/13552541111124743.

[18] D. I. Stoia, E. Linul, and L. Marsavina, "Influence of manufacturing parameters on mechanical properties of porous materials by selective laser sintering," *Materials*, vol. 16, no. 6, 2019, doi: 10.3390/ma12060871.

[19] G. Savio, R. Meneghello, and G. Concheri, "Design of variable thickness triply periodic surfaces for additive manufacturing," *Progress in Additive Manufacturing*, vol. 4, no. 3, pp. 281–290, 2019, doi: 10.1007/s40964-019-00073-x.

[20] NTopology, "Platform," 2020, *New York*.

[21] Altair Inc., "Altair HyperMesh," 2023.

[22] I. E. Ramirez-Chavez *et al.*, “Strain Redistribution in Stochastically Perturbed Single and Dual-Phase Cellular Materials Under Quasistatic Compression,” *Manuf. Lett.*, no. 41, pp. 1034–1045, 2024, [Online]. Available: www.sciencedirect.com

[23] L. Bai, C. Yi, X. Chen, Y. Sun, and J. Zhang, “Effective design of the graded strut of BCC lattice structure for improving mechanical properties,” *Materials*, vol. 12, no. 13, 2019, doi: 10.3390/ma12132192.

[24] Y. Xiang, M. Wang, T. Yu, and L. Yang, “Key Performance Indicators of Tubes and Foam-Filled Tubes Used as Energy Absorbers,” vol. 7, no. 4, pp. 1–20, 2015, doi: 10.1142/S175882511550060X.

[25] nTopology [Online], “Next-Generation Design & Engineering Software | NTopology,” https://ntopology.com/.

[26] L. Wang, S. Tao, P. Zhu, and W. Chen, “Data-driven topology optimization with multiclass microstructures using latent variable Gaussian process,” *Journal of Mechanical Design, Transactions of the ASME*, vol. 143, no. 3, 2021, doi: 10.1115/1.4048628.

[27] T. Archer, “Procedurally Generating Terrain,” *44th annual midwest instruction and computing symposium, Duluth*, pp. 378–393, 2011.